Zhao *et al.*
Chinese Journal of Mechanical Engineering (2024) 37:100
https://doi.org/10.1186/s10033-024-01086-6

Chinese Journal of Mechanical Engineering

ORIGINAL ARTICLE

Open Access

Effect of Y on Oxidation Behavior of Directionally Solidified Ni-Based Single-Crystal Superalloy

Zihan Zhao[1], Kai Guan[1], Renjie Cui[1], Jianchao Qin[1] and Zhaohui Huang[1*]

Abstract

The effect of yttrium (Y) addition on the oxidation behavior of a Ni-based directionally solidified single-crystal superalloy is investigated in this study. Isothermal oxidation tests for samples with different levels of Y addition are conducted at 1100 °C in air. The Y content of the samples is determined by the actual pickup amount obtained from an Inductively Coupled Plasma-Atomic Emission Spectrometry test. It is discovered that the addition of Y increases the oxide resistance by the scale of an adhesive double-layer oxide, which is composed of Al_2O_3 and spinel $Ni(Cr,Al)_2O_4$. With 70 ppm of Y addition, the oxidation mass gain decreases from 12.6 g/m^2 for the alloy without Y addition to 5.3 g/m^2, and the oxidation rate decreases significantly. In addition, the internal nitride disappears after Y doping because of an increase in oxidation scale adherence and a decrease in oxidation products. In this study, the alloy with 660 ppm Y addition demonstrates the best oxidation resistance.

Keywords Isothermal oxidation, Element Y, Single-crystal superalloy, Oxide scale

1 Introduction

Nickel-based superalloys have been used as the main materials in the aerospace industry and industrial gas turbines owing to their excellent properties such as high strength, relatively low density, and high environmental resistance at high operating temperatures [1–3]. Turbines, such as high-pressure turbines or combustors, are exposed to high temperature and oxygen-enriched environments, which implies that they must be manufactured using materials of high mechanical properties [4, 5]. The oxidation resistance of alloys at high temperatures is primarily achieved by the formation of a passive oxide scale [6–8].

The addition of rare earth (RE) elements can reduce the amount of impurities in the melt form because of the active properties of RE, which significantly affect the oxidation resistance of the alloy through the formation of an adhesive protective oxide scale that has a low growth rate [9, 10]. In 1966, Francis and Whitlow first added yttrium (Y) to a Cr–Fe alloy, which was proven to improve the oxidation resistance [11]. In the past decades, a number of studies have shown that the addition of RE elements to superalloys improved the oxidation resistance properties of alloys in high-temperature environments [12, 13].However, the mechanism associated with the effect of RE elements on the oxide scale remain ambiguous. Several researchers deduced that Y doping can result in better scale adhesion because of the "tying up" effect on S by RE elements [14]. However, all the sulfide-forming cases were based on the premise that the alloy involved had high sulfur activity and low oxygen activity. Furthermore, that sulfides could not be observed in the alloy were considered as well. From another viewpoint, RE elements would "site block"

*Correspondence:
Zhaohui Huang
huangzhaohui621@163.com
[1] Science and Technology on Advanced High Temperature Structural Materials Laboratory, Beijing Institute of Aeronautical Materials, Beijing 100095, China

at the grain boundaries to inhibit the outward diffusion of Al^{3+} [15]. Recently, Heuer and Hovis proposed a new perspective, i.e., REs might affect the oxidation behavior by reducing both the diffusion of O^{2-} to the grain boundaries and the Al ionization [16].

In this study, different amounts of Y were added to a directionally solidified nickel-based single-crystal superalloy to investigate the effect of Y addition on the oxidation behavior.

2 Experimental Details

A second-generation nickel-based single-crystal ziroy sample with a composition of Ni-7.5Co-7.0Cr-6.2Al-6.5Ta-5.0W-1.5Mo-3.0Re-0.15Hf-0.05C-0.04B (wt%) and different Y doping levels were used in this study.

[001]-oriented single-crystal bars were prepared using an industrial Bridgeman directional solidification furnace, in which the Y level was changed using different amounts of Ni–Y intermediate alloy. Single-crystal bars were subjected to standard heat treatment. The Inductively Coupled Plasma-Atomic Emission Spectrometry results show that the final pick-up amounts of Y were 70, 190, 230, and 660 ppm, and the corresponding specimens were labeled as 0Y, 70Y, 190Y, 230Y, and 660Y, respectively. The specimens for the isothermal oxidation experiment were cut into pieces measuring 30 mm × 10 mm × 1.5 mm from these single-crystal bars via electron spark machining, and then polished using a series of SiC paper up to 800-grit. The specimens were cleaned with alcohol, followed by dry blowing.

The tested specimens were heated in dry and static air at 1100 °C for 100 h, and during the testing, they were weighed at intervals of 25 h. An X-ray diffractometer was used to characterize the oxide scales on the sample surface. The microstructures of the oxide scales and element distributionmaps were analyzed using a field-emission scanning electron microscope equipped with an energy dispersive spectrometer. The surface roughness was determined using a laser-scanning confocal microscope.

During the isothermal oxidation experiment, the weight of the porcelain crucible was recorded before oxidation (m_1) and after every oxidation interval (m_2). The mass gain per unit of oxidation (G^+) and the average oxidation rate ($\overline{K^+}$) were calculated as follows:

$$G^+ = \frac{m_2 - m_1}{S},$$

$$\overline{K^+} = \frac{\overline{G^+}}{t}.$$

3 Oxidation Kinetics

For the Ni-based superalloy, during the initial stage of isothermal oxidation, the instantaneous oxidation products first formed a spinel $Ni(Al,Cr)_2O_4$ and NiO layer at the alloy surface, and the various oxide contents of the oxide scale was determined by the composition of alloy. At this stage, the contribution of element diffusion to the oxidation process was insignificant. As the oxidation process reached the steady state, element diffusion began dominate the oxidation process. Under the initial oxide layer, a continuous Al_2O_3 or Cr_2O_3 layer was formed, which was determined by the composition of the alloy. It is widely recognized that the addition of RE elements can improve the oxidation resistance of Ni-based superalloys. The Y-doped alloys showed clear differences in the 0Y sample. Compared with the 0Y sample, Y doping reduced the oxidation rate and the total mass gain after 100 h of isothermal oxidation.

As shown in Figure 1(a), among all the samples, sample 0Y indicated the maximum mass gain, and the value after oxidation for 100 h was 12.6 g/m^2. Compared with sample 0Y, samples 70Y, 190Y, 230Y, and 660Y indicated a monotonically decreasing mass gain of 5.3, 5.5, 5.2, and 4.1 g/m^2, respectively. Sample 660Y indicated the least mass gain after 100 h of oxidation, which was approximately one-third that of sample 0Y. Additionally, Figure 1(a) clearly shows that, compared with 0Y, at the earlier stage, the Y-doped alloy approached a steady state of mass gain. During the first 25 h of oxidation, the mass gain between each Y-doped specimen did not differ significantly. Compared with the Y-doped alloy, sample 0Y exhibited a high mass gain even after 25 h of testing. Based on the regression analysis results of the isothermal oxidation test data, the oxidation tendency of sample 0Y obeyed the parabolic law, and the oxidation behavior of the Y-doped samples reflected the cubic law. The change in the oxidation rules implied that the Y-doped alloy had a higher oxidation resistance than the 0Y alloy. The square of the mass gain of sample 0Y vs. the test time is plotted in Figure 1(b), and the parabolic oxidation rate constant, K_p, was 1.785 g^2/m^4h. Figure 1(c) shows the cubic mass gain vs. test time; the K_p values of samples 70Y, 190Y, 230Y, and 660Y were 1.480, 1.605, 1.445, and 0.656 g^3/m^6h, respectively. The K_p value of sample 70Y was approximately 2.5 times that of sample 660Y, which implied that 660 ppm was the best addition amount for Y to increase the oxidation resistance of the alloy in this study.

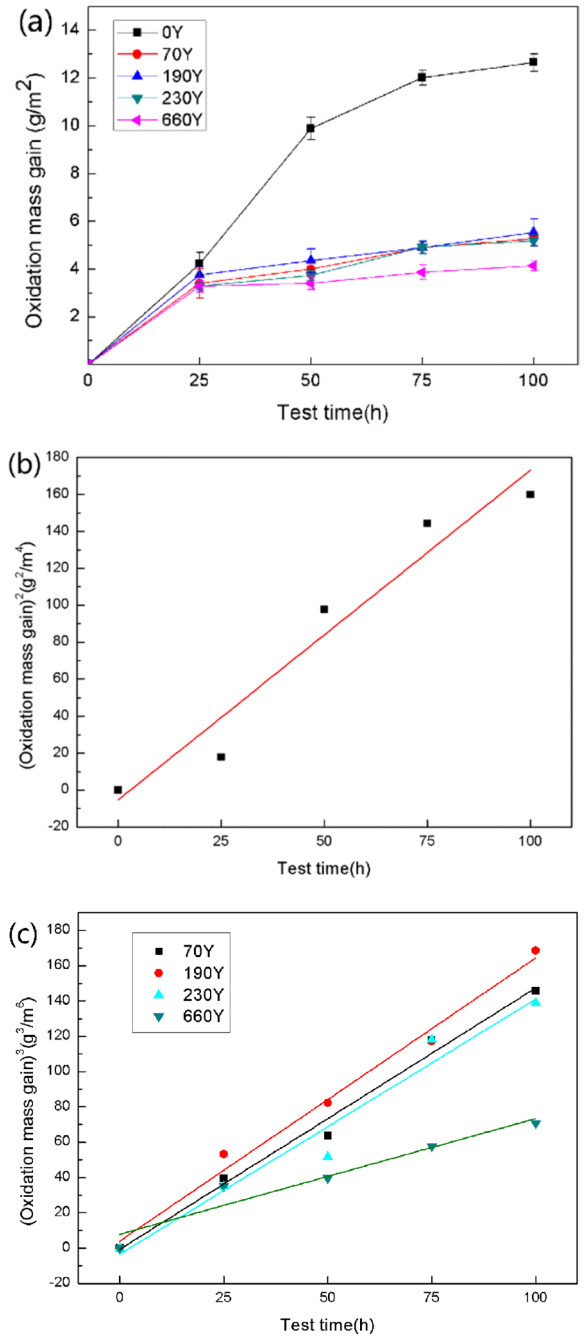

Figure 1 Oxidation kinetics of isothermal oxidation at 1100 °C for 100 h for Ni-based single-crystal superalloy samples with different amounts of Y addition: (**a**) Change in oxidation mass gain, (**b**) (Oxidation mass gain)^2 vs. test time for sample 0Y, (**c**) (Oxidation mass gain)^3 vs. test time for Y-doped samples

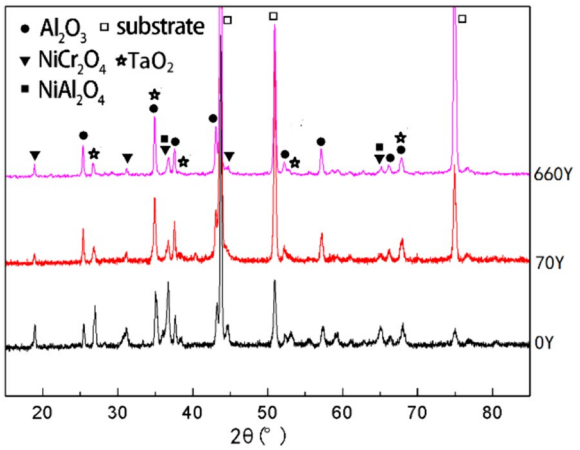

Figure 2 XRD pattern of oxide sale formed on samples with different Y addition amounts after oxidation at 1100 °C for 100 h

The phase substituents of the samples after oxidation are shown in Figure 2. The oxidation products primarily comprised Al_2O_3, $Ni(Cr,Al)_2O_4$, and TaO_2. The Al_2O_3 and TaO_2 peaks between the different samples did not change significantly; however, the peak strengths of the $Ni(Cr,Al)_2O_4$ phases weakened in the Y-doped samples, signifying a possible decrease in the amount of formed $Ni(Cr,Al)_2O_4$ compared with the 0Y sample. The EDS mapping results of the 0Y and 70Y oxide scales proved this hypothesis. A $Ni(Cr,Al)_2O_4$ layer is evident in Figure 3(a), whereas such a layer is not shown in Figure 3(b).

4 Oxidation Scale

Figure 4(a–e) show the surface morphologies of the different Y-doped alloys after oxidation at 1100 °C for 100 h. Cubic oxides appeared on the surface of sample 0Y. For sample 70Y, the cubic morphology of the oxidation particles on the alloy surface disappeared, and the oxidation particles were ridged and arranged compactly. As the Y content increased, the ridged particles began to agglomerate into a cauliflower-like bulge. When the agglomerates grew continuously, the distance between each agglomerate became smaller. Based on the EDS analysis (Table 1), the main composition of the oxide scale at the surface of all the samples was Al_2O_3, whereas a small amount of $Ni(Al,Cr)_2O_4$ was indicated as well.

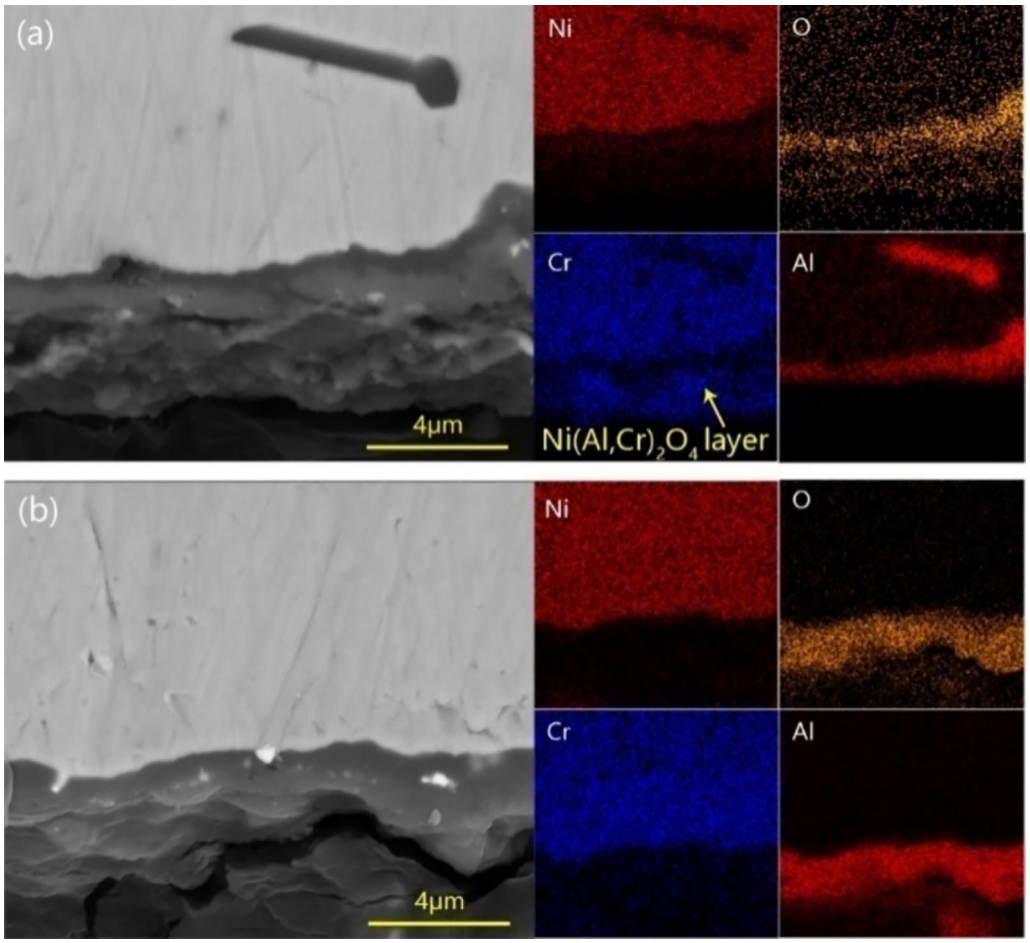

Figure 3 Element area distribution maps of oxide scale: (**a**) 0Y, (**b**) 70Y

Figure 5 shows the height histogram of the oxide surface, which can intuitively reflect the roughness of the sample surface; the higher the number of particles detected, the rougher is the sample surface.

It was discovered that, compared with 0Y, the roughness of 70Y decreased. For all Y-added alloys, the roughness of the oxide surface first increased and then decreased. The variation in the roughness resulting from the height histogram was consistent with the change tendency of the surface morphologies shown in Figure 4. As more Y was added, the oxide on the surface of the samples first increased and then gradually agglomerated into a uniform and continuous state.

As shown in Figure 6, all the Y-doped specimens had a continuous Al_2O_3 oxide scale, indicating better oxidation resistance than the alloy without Y addition. This enhancement is similarly reflected in the low dropping weight of the oxide scale compared with that of 0Y (as shown in Figure 7).

Figure 8 shows the oxide scale structure of sample 230Y, which represents the typical oxide scale structure of the Ni-based alloy investigated in this study. Based on the EDS and XRD analysis results (shown in Figure 2), it exhibited a double-layer structure; the outer and inner layers were composed of $Ni(Al,Cr)_2O_4$ and Al_2O_3, respectively.

The difference in oxide scale between samples 0Y and 660Y is depicted clearly shown in Figure 9(a) and (b). A needle-like phase appeared near the oxide scale in sample 0Y; combined with the chemical composition of Points 3 and 4 denoted in Figure 9(c) and Table 2, these needle-like phases were identified as AlN. In sample 660Y, the

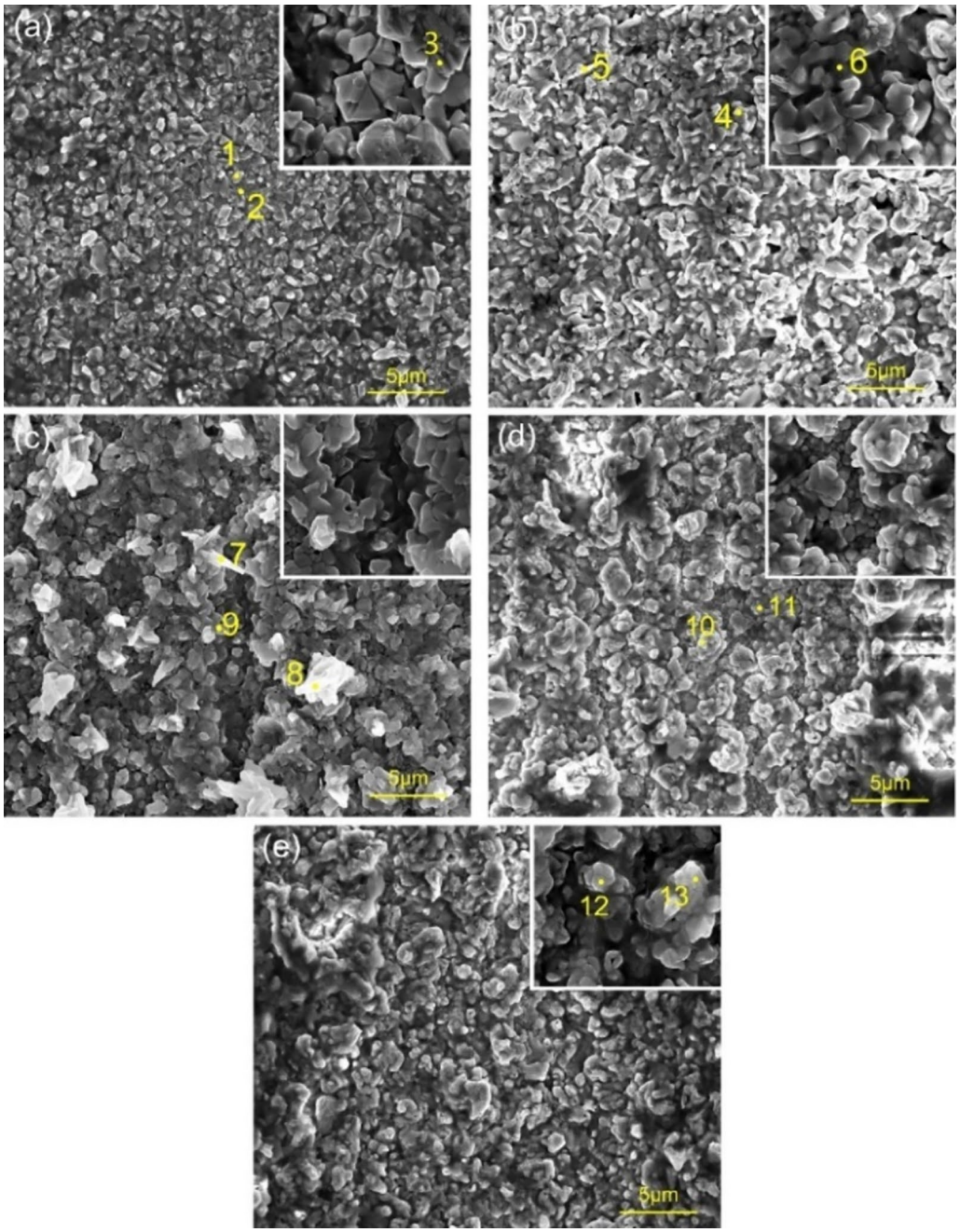

Figure 4 Morphology of surface oxidation scale of alloy with different Y contents after oxidation at 1100 °C: (**a**) 0Y, (**b**) 70Y, (**c**) 190Y, (**d**) 230Y, and (**e**) 660Y

AlN phases disappeared. Based on the EDS mapping shown in Figure 9(c), the oxide scale of sample 0Y can be categorized into two layers. Based on the data in Table 2, layers 1 and 2 corresponded to the $Ni(Al,Cr)_2O_4$ and Al_2O_3 layers, respectively. However, only the Al_2O_3 layer was present in sample 660Y; in other words, the $Ni(Al,Cr)_2O_4$ layer was no longer visible in sample 660Y.

Table 1 Chemical composition of points shown in Figure 4 (at. %)

Point	Chemical composition (at.%)							Deduced phases
	C	O	Al	Cr	Co	Ni	Fe	
1	31.81	38.85	23.35	1.85	0.63	3.51	–	Al_2O_3
2	27.59	43.28	22.78	1.84	0.69	3.83	–	Al_2O_3
3	20.29	40.47	5.16	15.56	2.59	15.93	–	$Ni(Al,Cr)_2O_4$
4	10.03	42.43	28.86	2.41	–	16.27	–	$Ni(Al,Cr)_2O_4$
5	14.93	51.58	22.16	1.64	–	9.69	–	$NiAl_2O_4$
6	30.54	45.39	24.07	–	–	–	–	Al_2O_3
7	16.41	54.02	23.8	1.16	0.81	3.71	0.08	Al_2O_3
8	20.72	48.18	25.65	1.24	0.79	3.42	–	Al_2O_3
9	–	62.3	36.57	0.45	0.11	0.58	–	Al_2O_3
10	–	59.49	37.89	0.97	0.28	1.37	–	Al_2O_3
11	16.33	52.17	30.06	0.58	0.13	0.73	–	Al_2O_3
12	–	62.42	35.67	0.71	0.17	1.04	–	Al_2O_3
13	25.14	47.38	22.23	1.06	0.73	3.46	–	Al_2O_3

Based on the cross-section of the oxide scale, a nail-like internal oxidation pattern was observed within the Y-doped specimens, as shown in Figure 10. Meanwhile, the EDS analysis results in Table 3 show that, from the inside to outside, the "nail" was composed of Al_2O_3, a mixture of refractory oxides/carbides, and an oxide containing Y. Furthermore, it was clear that the oxide containing Y was located at the bottom of the "nail".

Table 4 shows the change in the oxide scale thickness, spallation amount of oxide scale, and oxidation mass gain for different samples. Sample 660Y indicated the smallest oxide scale thickness, i.e., approximately one-half that of sample 0Y. Meanwhile, sample 660Y indicated the least spallation amount and oxidation mass gain among the five types of samples. Therefore, it can be concluded that the 660Y alloy samples exhibited the best oxidation resistance among all the Y-doped samples.

5 Discussion

The initial oxidized products were NiO and spinel ($Ni(Cr,Al)_2O_4$), in which NiO first formed during the oxidation process but eventually disappeared as the intermediate product because it reacted with Al_2O_3 and Cr_2O_3 to form $Ni(Cr,Al)_2O_4$ [17, 18]. This can be described by the following expression [19]:

$$NiO + Cr_2O_3/Al_2O_3 \rightarrow Ni(Al,Cr)_2O_4.$$

Owing to the addition of Y, oxide scale spallation almost disappeared, which resulted in a significant increase in the oxidation resistance of the alloy.

According to the classic Wagner theory, the oxidation process is orientational and determined by the direction of ion diffusion [20, 21]. Subsequently, based on a study pertaining to NiCrAls and FeCrAls, oxide scale formation involves both outward aluminum diffusion and inward oxygen diffusion, and the pathway of the oxidizing process is along the grain boundaries [22, 23].

An analysis of the oxidation kinetic curves show that the oxidation resistance increased with the addition of Y, and the addition of 660 ppm yielded the best oxidation resistance. However, considering the possible adverse effect of excessive amounts of Y on the comprehensive properties of Ni-based single-crystal superalloys [24, 25], Y amounts exceeding 660 ppm were not investigated in this study.

The segregation of Y ions would occur at the matrix/oxide scale interface because of the high chemical activity of element Y [26]. Because of the higher standard Gibbs free energy (ΔG^{θ}) of Y_2O_3, the affinity of Y with O was stronger than that of C with Al [24, 27]; hence, Y_2O_3 formed at the surface prior to the Al_2O_3 layer. It was demonstrated that Y_2O_3 is suitable as the core particle for Al_2O_3 formation and hence promotes the formation of an oxide scale [28]. The continuous oxide scale formed

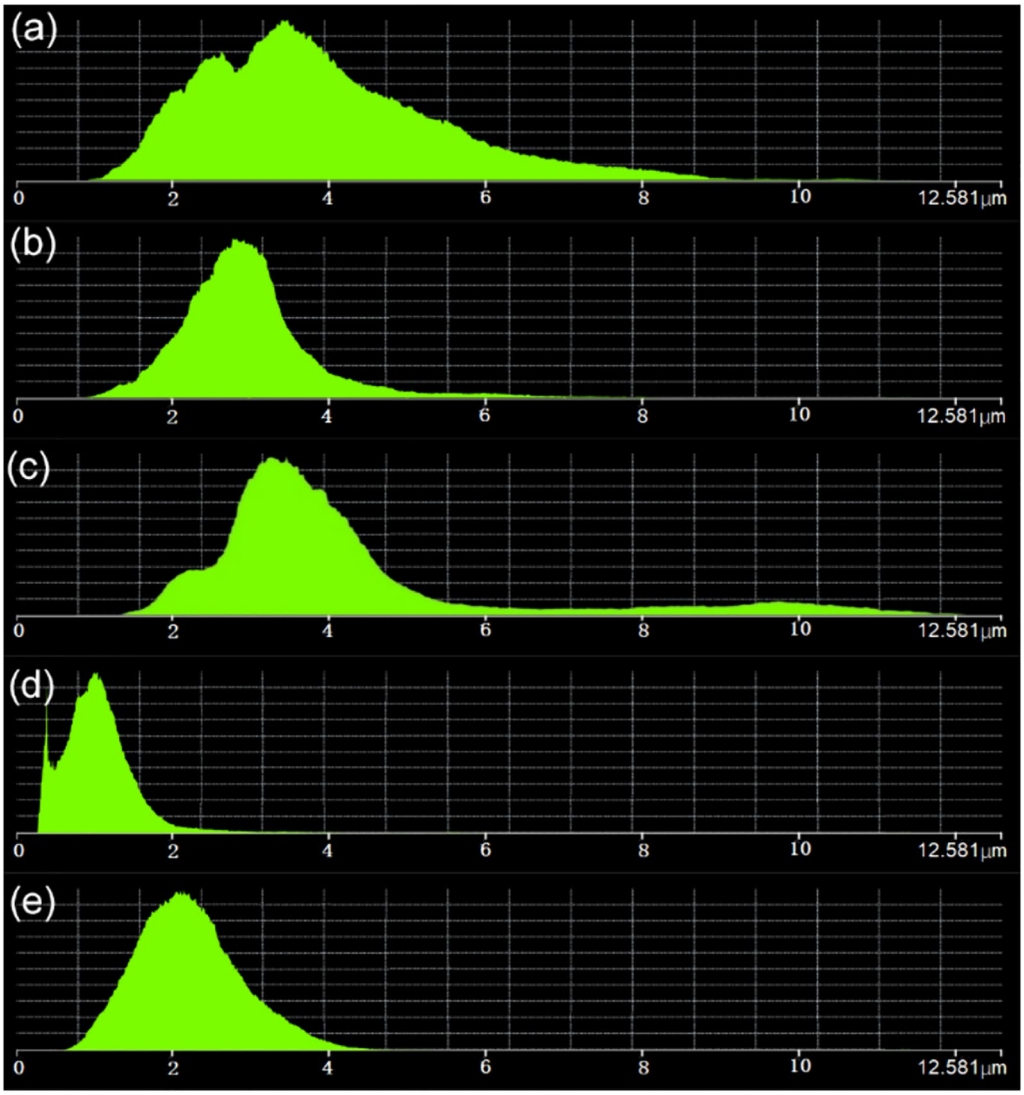

Figure 5 Height histogram results obtained from laser scanning confocal microscopy test: (**a**) 0Y, (**b**) 70Y, (**c**) 190Y, (**d**) 230Y, (**e**) 660Y

rapidly, thereby inhibiting the formation of $Ni(Al,Cr)_2O_4$. It appeared that he formation of Y_2O_3 affected the Al^{3+}/O^{2-} diffusion behavior at the grain boundaries [13, 20, 29]. In this study, the oxide particles containing Y, to some extent, should exhibit functions similar to Y_2O_3, as shown in Figure 11. In this case, the diffusion behavior was weakened owing to the obstruction of the oxide containing Y at the diffusion pathway. Consequently, the Al_2O_3 thickness reduced, but no evidence of significant segregation between Al^{3+} and O^{2-} was discovered. This might cause both the spinel layer and Al_2O_3 layer of the 660Y sample to be thinner than those of sample 0Y.

For sample 0Y, needle-like aluminum nitrides appeared at the near-surface region of the oxidation scale in the matrix. Owing to the volume increase, which was caused

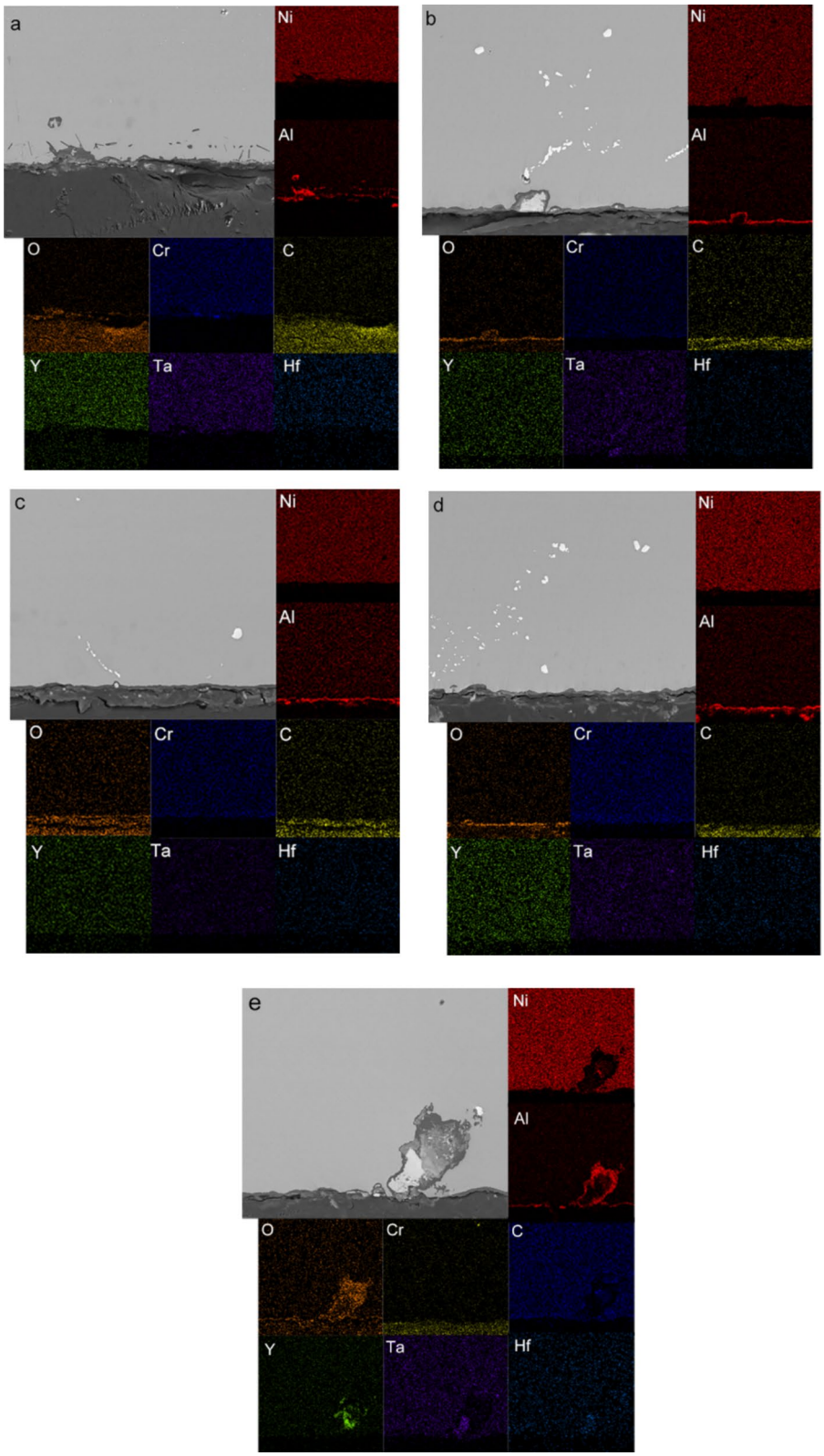

Figure 6 Section morphologies of oxide scale and element area distribution maps of Ni-based superalloy after oxidation at 1100 °C for 100 h: (**a**) 0Y, (**b**) 70Y, (**c**) 190Y, (**d**) 230Y, (**e**) 660Y

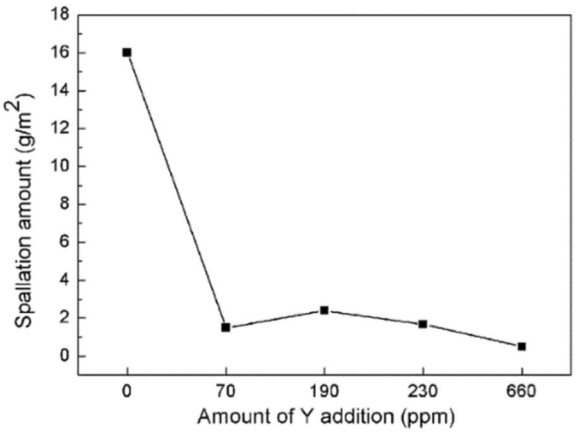

Figure 7 Spallation amount of oxide scale with different amounts of Y addition

by the formation of the oxides (Al_2O_3 28% increase) [30], cracks and spallation occurred [31]. Cracks were observed across the oxide scales, and N further penetrated through the cracks to form AlN. However, owing to Y doping, the aluminum nitrides disappeared because of the greater oxide scale adherence and fewer oxidation products, as well as a lower volume increase below the oxide scale, and the cracks disappeared [32]. By contrast, as reported in other published studies [33, 34], this phenomenon is associated with the purification of the alloy after the addition of Y.

6 Conclusions

Based on the investigation of the oxidation kinetics and surface/cross-sectional morphologies of the oxidation scale, some key points can be summarized as follows:

(1) To improve the oxidation resistance of Ni-based superalloys, doping with Y effectively decreased the oxidation rate, and after oxidation at 1100 °C for 100 h, the mass gain of the 70 ppm Y alloy decreased from 12.6 to 5.3 g/m^2. Furthermore, the 660Y alloy exhibited the lowest mass gain, spallation amount, and oxide scale thickness. Therefore, in this study, theoptimal Y content was 660 ppm.

(2) The alloy investigated in this study was Al_2O_3 formation alloy, which has a typical double-layer structure of the oxide scale, where one layer contained Al_2O_3 and $Ni(Al,Cr)_2O_4$ spinel primarily, whereas the other layer contained oxide/carbide particles of refractory elements.

(3) Y addition into the Ni-based single-crystal superalloy resulted in a Y-containing adhesive oxide scale, which decreased the thickness of both the outermost $Ni(Al,Cr)_2O_4$ layer and inner Al_2O_3 layer.

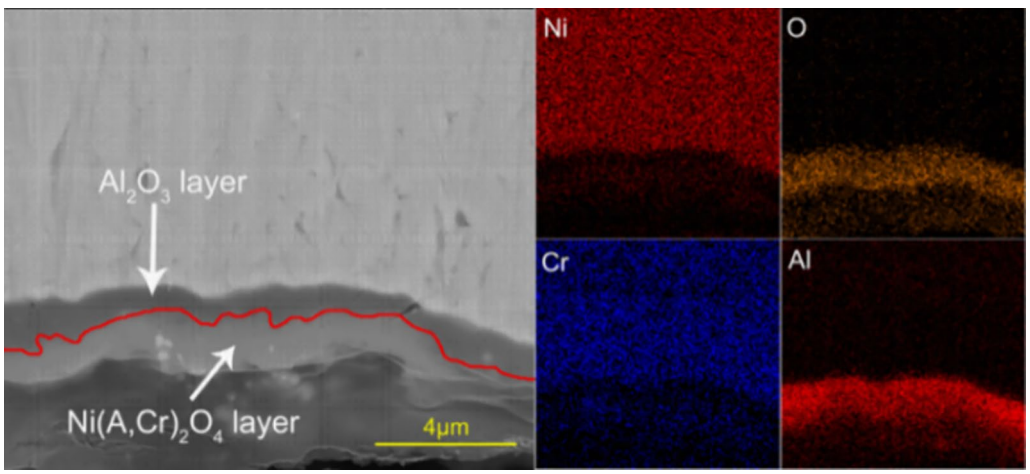

Figure 8 Double-layer structure of oxide scale (230 ppm Y-doped sample)

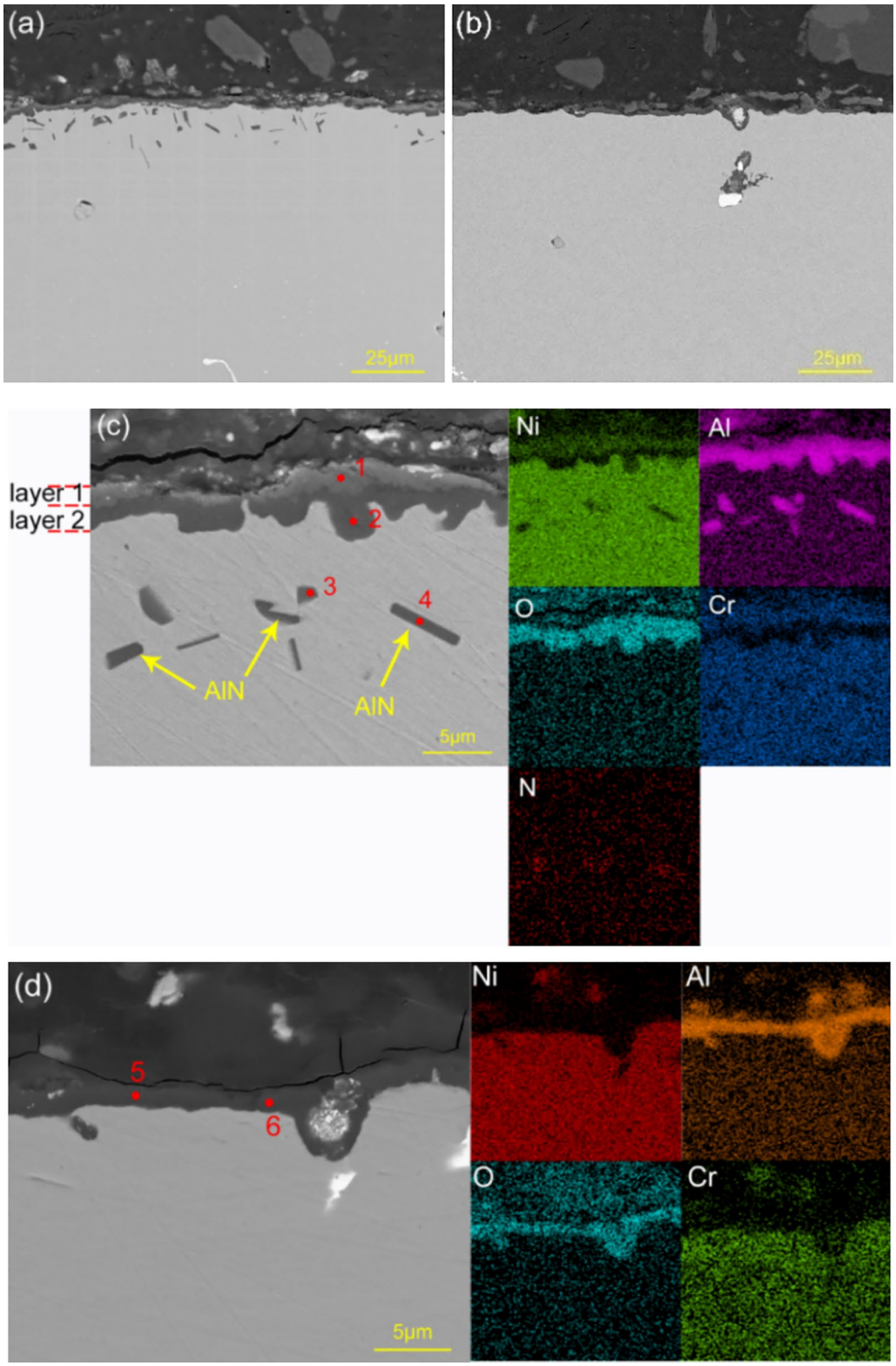

Figure 9 Section morphologies of oxide scale: (**a**) 0Y, (**b**) 660Y, (**c**) 0Y, (**d**) 660Y

Table 2 Chemical composition of points shown in Figure 9 (at. %)

Point	Chemical composition (at.%)							Deduced phases
	O	Al	N	Cr	Ni	Co	C	
1	36.54	21.95	–	2.29	9.5	1.48	28.24	$Ni(Al,Cr)_2O_4$
2	38.12	31.96	–	1.09	5.51	0.89	22.44	Al_2O_3
3	1.82	24.32	22.38	2.84	21.25	2.97	24.42	AlN
4	–	35.71	26.57	1.4	10.68	1.52	24.13	AlN
5	39.36	25.82	–	1.04	3.63	0.63	29.51	Al_2O_3
6	39.96	27.76	–	0.5	2.62	0.43	28.72	Al_2O_3

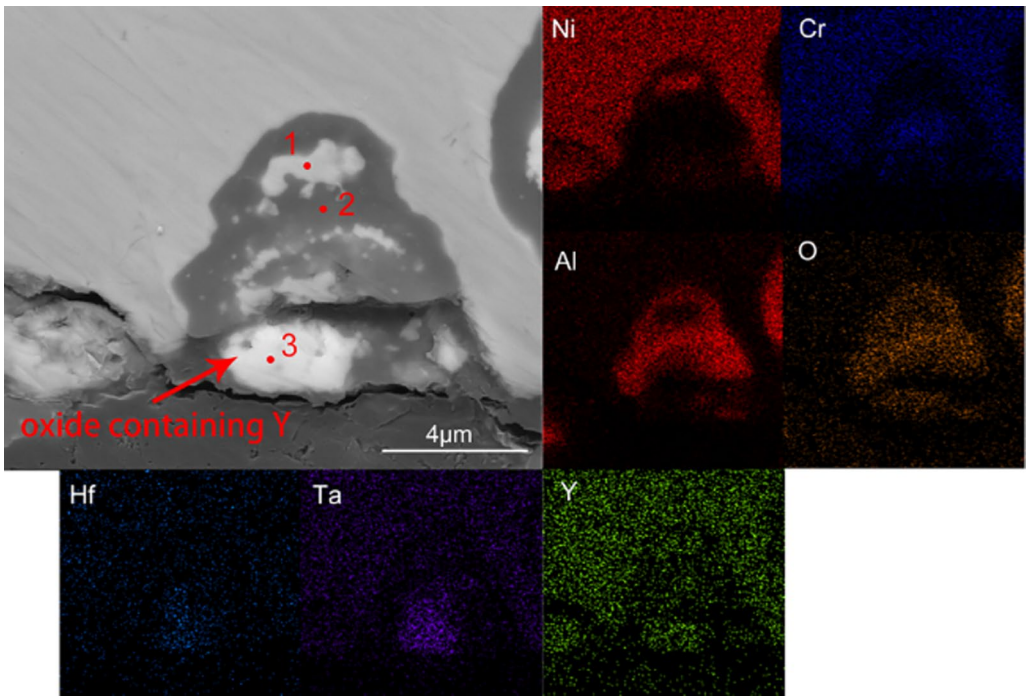

Figure 10 Typical section morphologies of oxide scaleand element area distribution maps of nail-like internal oxide in 660Y sample

Table 3 Chemical composition of points shown in Figure 10 (at. %)

Point	Chemical composition (at.%)													Deduced phases
	C	N	O	Al	Si	Ti	Cr	Co	Ni	Y	Hf	Ta	Re	
1	45.47	–	7.18	6.91	2.55	0.06	1.07	5.28	30.67	–	–	–	0.81	Substrate
2	40.49	1.4	30.85	19.83	0.76	0.03	1.84	0.58	3.46	–	0.13	0.43	0.19	Al_2O_3
3	33.95	–	36.53	2.88	4.52	0.09	1.58	0.97	5.91	0.23	1.54	11.04	0.78	Oxide containing Y&Ta

Table 4 Characteristics of oxide scale for different amounts of Y addition

	0Y	70Y	190Y	230Y	660Y
Thickness of oxide scale (μm)	3.698	2.799	1.987	2.435	1.882
Spallation amount (g/m^2)	16.000	1.500	2.400	1.683	0.500
Oxidation mass gain (g/m^2)	12.645	5.264	5.525	5.180	4.135

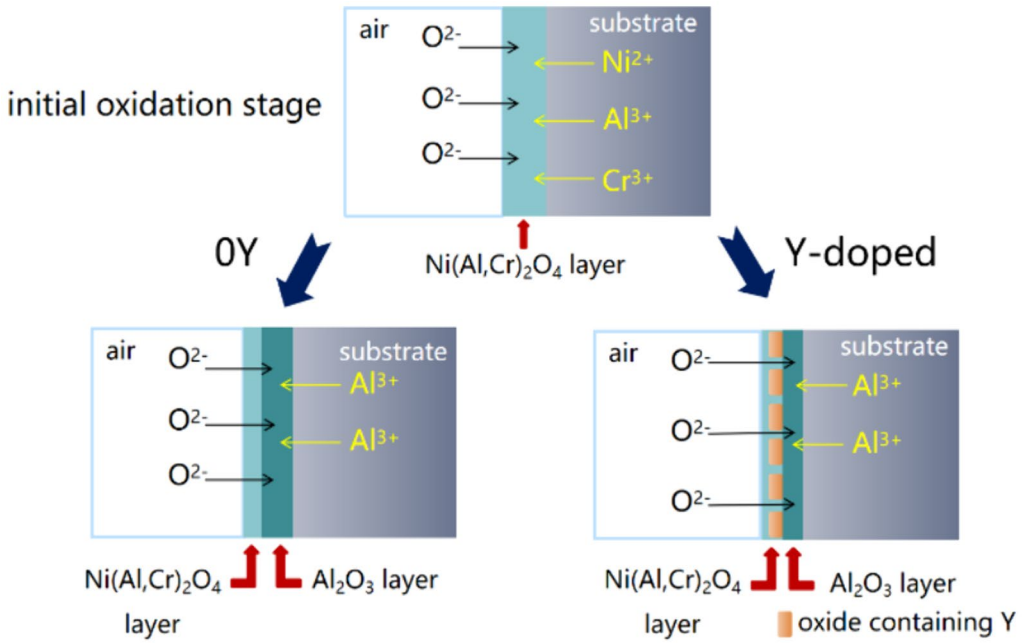

Figure 11 Oxidation mechanism of 0Y and Y-doped samples

Consequently, the oxide volume decreased, and cracks disappeared in the oxide scale.

Received: 21 July 2024 Revised: 21 July 2024 Accepted: 29 July 2024
Published online: 03 September 2024

Acknowledgements
Not applicable.

Authors' Contributions
ZHZ and KG were in charge of the whole trial; ZHZ wrote the manuscript; RJC and JCQ assisted with sampling and laboratory analyses; ZHH assisted with the revision. All authors read and approved the final manuscript.

Funding
Supported by Preliminary Research Project of China (Grant No. J2019-VI-0023).

Availability of Data and Materials
The datasets used and/or analysed during the current study are available from the corresponding author on reasonable request.

Declarations

Competing Interests
The authors declare no competing financial interests.

References

[1] R Darolia. Development of strong, oxidation and corrosion resistant nickel-based superalloys: critical review of challenges, progress and prospects. *International Materials Reviews,* 2019, 64(6): 355-380.
[2] H Pei, Z Wen, Y Zhang, et al. Oxidation behavior and mechanism of a Ni-based single crystal superalloy with single α-Al2O3 film at 1000°C. *Applied Surface Science,* 2017, 411: 124-135.
[3] D V V Satyanarayana, N Eswara Prasad. Nickel-based superalloys. In: N E Prasad, R J H Wanhill, eds. *Aerospace materials and material technologies : Volume 1: Aerospace materials,* 2017: 199–228. Singapore: Springer Singapore.
[4] M Ansari, R Shoja-Razavi, M Barekat, et al. High-temperature oxidation behavior of laser-aided additively manufactured NiCrAlY coating. *Corrosion Science,* 2017, 118: 168-177.
[5] K Kraemer, L Woellmann, F Mueller, et al. On the corrosive behavior of nickel-based superalloys for turbine engines: Cyclic oxidation and its impact on crack propagation. *Joint EPRI – 123HiMAT International Conference on Advances in High Temperature Materials*, 2019.

[6] Y Zhang, H Luo, Q Zhong, et al. Characterization of passive films formed on as-received and sensitized AISI 304 stainless steel. *Chinese Journal of Mechanical Engineering,* 2019, 32: 27.
[7] H Zhang, Z Yang, Z Wu, et al. Oxide-scale evolution on a new Ni–Fe-based superalloy at high temperature. *Oxidation of Metals,* 2019, 92(1): 49–65.
[8] W Chen, X Shan, Y Guo, et al. The effect of reactive element species and concentrations on the isothermal oxidation of β-NiAl coating fabricated by spark plasma sintering. *Surface and Coatings Technology,* 2019, 357: 841-848.
[9] T B Guo, F Zhang, W W Ding, et al. Effect of micro-scale Y addition on the fracture properties of Al–Cu–Mn alloy. *Chinese Journal of Mechanical Engineering,* 2018, 31: 79.
[10] H Jin, A Felix. Influence of rare earth doping on mechanical property and micro-structure of chromia oxide film. *Chinese Journal of Mechanical Engineering,* 2008, 21(03): 16-19.
[11] J M Francis, W H Whitlow. The morphology of oxide film growth on AISI type 304 stainless steel in high temperature water at 300° and 350° C. *Journal of Nuclear Materials,* 1966, 20(1): 1-10.
[12] X Li, S He, J Liang, et al. High-temperature oxidation behavior and oxide scale structure of yttrium-modified Ni–16Mo–7Cr–4Fe superalloy at 1273 K. *Oxidation of Metals,* 2019, 92(1): 67–88.
[13] K Rehman, N Sheng, Z Sang, et al. Comparative study of the reactive elements effects on oxidation behavior of a Ni-based superalloy. *Vacuum,* 2021, 191: 110382.
[14] P R Aimone, R L McCormick. The effects of yttrium and sulfur on the oxidation resistance of an advanced single crystal nickel based superalloy. *Superalloys*, 1992: 817–823.
[15] D W Yun, S M Seo, H W Jeong, et al. The effect of Gd addition on the cyclic oxidation behavior and creep life of alumina-forming Ni-based superalloy. *Corrosion Science,* 2020, 170: 108694.
[16] A Heuer, D Hovis, J Smialek, et al. Alumina scale formation: A new perspective. *Journal of the American Ceramic Society,* 2011, 94(s1): 2698–2698.
[17] L Chen, H Luo, Z Li, et al. Effect of Al doping on the early-stage oxidation of Ni-Al alloys: A ReaxFF molecular dynamics study. *Applied Surface Science,* 2021, 563: 150097.
[18] L Zhao, Y Tan, S Shi, et al. High temperature oxidation behavior of electron beam smelted K417 superalloy. *Vacuum,* 2019, 170: 108979.
[19] M Bensch, A Sato, N Warnken, et al. Modelling of high temperature oxidation of alumina-forming single-crystal nickel-base superalloys. *Acta Materialia,* 2012, 60(15): 5468–5480.
[20] A H Heuer, T Nakagawa, M Z Azar, et al. On the growth of Al_2O_3 scales. *Acta Materialia,* 2013, 61(18): 6670-6683.
[21] M P Tautschnig, N M Harrison, M W Finnis. A model for time-dependent grain boundary diffusion of ions and electrons through a film or scale, with an application to alumina. *Acta Materialia,* 2017, 132: 503-516.
[22] K A Unocic, Y Chen, D Shin, et al. STEM and APT characterization of scale formation on a La, Hf, Ti-doped NiCrAl model alloy. *Micron,* 2018, 109: 41-52.
[23] J Jedlinski, J L G Poussard, J Dabek, et al. The effect of implanted Al and/or Y on the scale formation on low-Al Fe20Cr2Al alloy. *Oxidation of Metals,* 2017, 88(3): 371–382.
[24] Q-l Li, H-r Zhang, M Gao, et al. Mechanisms of reactive element Y on the purification of K4169 superalloy during vacuum induction melting. *International Journal of Minerals, Metallurgy, and Materials,* 2018, 25(6): 696-703.
[25] K Guan, Z Huang, R Cui, et al. Effects of yttrium on microstructure and mechanical properties of a directionally solidified single crystal superalloy. *Materials Science and Engineering: A,* 2019, 752: 86-92.
[26] Y Yang, T Zhang, Y Shao, et al. New understanding of the effect of hydrostatic pressure on the corrosion of Ni–Cr–Mo–V high strength steel. *Corrosion Science,* 2013, 73(aug.): 250-261.
[27] W Bian, H Zhang, X Zhang, et al. Comprehensive effect of Y on K417 superalloy: Purification, interactions among the alloy elements and high temperature properties. *Materials Science and Engineering A,* 2019, 755(MAY 7): 190-200.
[28] X Xiao, L Xu, X Z Qin, et al. Effect of elements Y and Ce on high temperature oxidation behavior of directionally-solidified Ni-based superalloy. *The Chinese Journal of Nonferrous Metals,* 2014, 24(11): 2769-2776.
[29] N Birks, G H Meier, F S Pettit. *Introduction to the high temperature oxidation of metals* (2 ed.). Cambridge: Cambridge University Press, 2006.
[30] A Pfennig, B Fedelich. Oxidation of single crystal PWA 1483 at 950 °C in flowing air. *Corrosion Science,* 2008, 50(9): 2484-2492.
[31] D Saber, I S Emam, R Abdel-Karim. High temperature cyclic oxidation of Ni based superalloys at different temperatures in air. *Journal of Alloys and Compounds,* 2017, 719: 133-141.
[32] A Chyrkin, R Pillai, T Galiullin, et al. External α-Al_2O_3 scale on Ni-base alloy 602 CA. – Part I: Formation and long-term stability. *Corrosion Science,* 2017, 124: 138-149.
[33] A V Guimarães, R M S D Silveira, L H D Almeida, et al. Effect of yttrium addition on the microstructural evolution and mechanical properties of superalloy 718. *Materials Science and Engineering A,* 2020, 776: 139023.
[34] W-d Bian, H-r Zhang, M Gao, et al. Effect of yttrium and vacuum degree on the purification of K417 superalloy. *Vacuum,* 2018, 152: 57-64.

Zihan Zhao born in 1996, is currently an assistant engineer at *Science and Technology on Advanced High Temperature Structural Materials Laboratory, Beijing Institute of Aeronautical Materials, China*. She received her master degree on Materials Science and Engineering from *AECC Beijing Institute of Aeronautical Materials, China,* in 2021. Her research interests include nickel-based superalloys.

Kai Guan born in 1988, is currently a senior engineer at *Science and Technology on Advanced High Temperature Structural Materials Laboratory, Beijing Institute of Aeronautical Materials, China*. He received his PhD degree on Materials Science and Engineering from *Beihang University, China*, in 2016.

Renjie Cui born in 1983, is currently a professor at *Science and Technology on Advanced High Temperature Structural Materials Laboratory, Beijing Institute of Aeronautical Materials, China*. He received his PhD degree on Materials Science and Engineering from *Beihang University, China*, in 2012.

Jianchao Qin born in 1993, is currently an engineer at *Science and Technology on Advanced High Temperature Structural Materials Laboratory, Beijing Institute of Aeronautical Materials, China*. He received his master degree on Materials Science and Engineering from *AECC Beijing Institute of Aeronautical Materials, China,* in 2017.

Zhaohui Huang born in 1968, is currently a professor at *Science and Technology on Advanced High Temperature Structural Materials Laboratory, Beijing Institute of Aeronautical Materials, China*. She received her PhD degree on Materials Science from *Jilin University of Technology, China*, in 1998.